TIME-DEPENDENT WATER VELOCITY INVERSION FROM OCEAN-BOTTOM NODE SEISMIC DATA

by

Tiago Santos Cabral

A thesis submitted to the Faculty and the Board of Trustees of the Colorado School of Mines in partial fulfillment of the requirements for the degree of Master of Science (Geophysics).

Golden, Colorado
Date _____

Signed: _____
Tiago Santos Cabral

Signed: _____
Dr. Paul Sava
Thesis Advisor

Golden, Colorado
Date _____

Signed: _____
Dr. Paul Sava
Professor and Head
Department of Geophysics

ABSTRACT

Time-lapse (4D) analysis is highly sensitive to small changes in the water column, which introduce traveltime shifts that can mask subtle reservoir signals. This thesis develops a tomographic framework to recover time-varying and spatially variable water-column velocity directly from ocean-bottom node (OBN) seismic data. The water velocity is parameterized as a function of space and calendar time and estimated by fitting first-arrival traveltimes with joint spatial and temporal regularization. A weighted pull-to-reference term incorporates prior knowledge about where variability is expected, while preserving background values in weakly illuminated regions. The resulting symmetric positive-definite normal equations are solved with a matrix-free, preconditioned conjugate gradient method.

Synthetic experiments demonstrate the method's effectiveness under realistic conditions. A moving Gaussian anomaly and a "field-inspired" model based on deep-water measurements both show that temporal regularization is essential for stabilizing the inversion in the presence of realistic pick noise ($\sim$1.5 ms, consistent with $\sim$meter-scale geometry uncertainty). Spatially varying weights further reduce vertical smearing and confine updates to the upper ocean where variability is concentrated. Reverse-time migration (RTM) tests indicate that using the recovered, spatially variable water models reduces 4D difference artifacts compared with using either no correction or a homogeneous water velocity, improving repeatability and the analysis of true subsurface changes.

This work contributes a practical route to mitigating water-column imprint in marine 4D seismic, particularly relevant for deep-water settings where reservoir responses can be weak. The framework is readily extensible to (i) full 3D geometry with multi-azimuth illumination, (ii) joint inversion of source/receiver positioning errors, and (iii) tighter integration of sound-velocity profiler and related oceanographic measurements as constraints. Collectively, these extensions promise further gains in 4D fidelity and more reliable reservoir monitoring.

TABLE OF CONTENTS

ABSTRACT iii

LIST OF FIGURES v

CHAPTER 1 INTRODUCTION 1

CHAPTER 2 TIME-DEPENDENT WATER VELOCITY INVERSION FROM OBN SEISMIC DATA 6

2.1 Abstract 6

2.2 Introduction 7

2.3 Theory 10

2.3.1 Problem Setup and Intuition 10

2.3.2 Inverse Problem Formulation 11

2.3.3 Numerical Solution of the Regularized Normal Equations 12

2.4 Numerical Examples 14

2.4.1 Gaussian Anomaly 15

2.4.2 Realistic Water Variation 17

2.5 Discussion 24

2.6 Conclusions 24

2.7 Acknowledgements 25

CHAPTER 3 SUMMARY AND FUTURE DIRECTIONS 26

REFERENCES CITED 29

LIST OF FIGURES

Figure 2.1 Idealized profiles of physical properties in the ocean water layer vs. depth, showing (left) increasing pressure, (middle) decreasing temperature in the thermocline, and (right) resulting non-monotonic acoustic velocity. 8

Figure 2.2 Water-layer acoustic velocity profiles acquired during field OBN surveys: (a) from the north-central part of the Green Canyon Protraction Area in the Gulf of Mexico (Seymour et al., 2021); (b) from the Tupi field in Brazil. The colored curves represent individual profiles at different locations and times, while the black curve shows the average profile. 9

Figure 2.3 Gaussian water-layer model used in the first experiment at calendar times: (a) 0 days and (b) 12 days. 13

Figure 2.4 3D representation of the Gaussian model. On the top, slices at $T = 1.1$ days, $T = 5.6$ days, $T = 10.1$ days. On the bottom, slice at depth $z = 2$ km. . . . 14

Figure 2.5 Inversion results for the Gaussian-anomaly experiment at $T \approx 3$ days. (a) True model regridded onto the inversion grid. (b) Spatial-regularization only, clean traveltimes. (c) Spatial-regularization only, noisy traveltimes. (d) Spatial + calendar-time regularization, noisy traveltimes. The white line denotes the water bottom. 16

Figure 2.6 Locations of discrete seismic velocity profiles measured during an OBN acquisition in the Santos Basin, Brazil: (a) colored by acquisition time and (b) colored by velocity value at depth 500 m. 17

Figure 2.7 Inversion results for the realistic water-velocity scenario at $T \approx 3$ days. (a) True model regridded to the inversion grid. (b) Spatial + calendar-time regularization (no depth weights). (c) Same regularization with spatially varying depth weights that favor updates above ~ 1 km. The white line denotes the water bottom. 19

Figure 2.8 3D representation of the inverted result from the realistic water-velocity scenario where varying depth weights were used. On the top, slices at $T = 1.1$ days, $T = 5.6$ days, $T = 10.1$ days. On the bottom, slice at depth $z = 600$ m. . . 20

Figure 2.9 Sigsbee velocity model used for the imaging experiments. 21

Figure 2.10 RTM difference images (inverted minus reference) using water layers from: (a) a spatially homogeneous but time-varying water velocity, (b) inversion without depth weights, and (c) inversion with shallow-favoring depth weights. The red box highlights the region of interest where the NRMS metric is computed. 22

Figure 2.11 RTM difference images (inverted minus reference), zoomed into the region of interest where the NRMS metric is computed. The water layers used for migration are: (a) a spatially homogeneous but time-varying water velocity, (b) inversion without depth weights, and (c) inversion with shallow-favoring depth weights. 23

CHAPTER 1

INTRODUCTION

Seismic reflection surveys have long been an important tool in geophysical exploration, providing detailed images of subsurface structures. By repeating seismic surveys over the same area at different times (a technique known as time-lapse or 4D seismic), geophysicists can monitor changes in the subsurface over the life of a reservoir. The differences between a baseline survey and subsequent "monitor" surveys reveal dynamic processes such as fluid movement, pressure depletion, or injection effects in hydrocarbon reservoirs (Wang et al., 2015). This makes 4D seismic a powerful tool for reservoir management, as it offers direct insights into how a reservoir is responding to production or injection.

For example, changes in seismic travel times or reflection amplitudes can indicate saturation changes due to brine replacing hydrocarbons, how pressure is propagating through the field, or if unexpected bypassed hydrocarbon zones remain. Such information helps reservoir engineers and geologists optimize well placement, enhance recovery, and avoid or minimize risks by observing the reservoir in action rather than just inferring from static models.

The value of 4D seismic hinges on the surveys being highly repeatable—that is, acquired and processed in a consistent manner so that any differences in the data truly reflect subsurface changes and not artifacts of calendar variations in seismic acquisition (e.g. survey geometry). In practice, achieving perfect repeatability is challenging. Even with careful survey planning, small differences in source or receiver positions, environmental conditions, and acquisition parameters between surveys can introduce differences unrelated to the reservoir. These unintended differences are often referred to as "4D noise" or non-repeatability noise (Mahgoub et al., 2023; Araujo et al., 2024). They can easily obscure the subtle signals of true reservoir change, especially in cases where the reservoir's 4D response is weak.

A prime example is in carbonate reservoirs, where the rock's stiff frame makes seismic properties relatively insensitive to fluid or pressure changes. The genuine 4D signal in carbonates is often so small that it can be lost beneath the noise floor (Lumley et al., 2005). In such scenarios, ensuring repeatable acquisition and removing non-reservoir differences are absolutely critical for successful 4D interpretation.

Over the past two decades, the industry has developed various strategies to maximize repeatability. On land and in shallow water, permanent monitoring systems (with buried or ocean-bottom cables) keep sensors in fixed positions. Offshore, one increasingly popular approach is to use ocean-bottom nodes (OBN) instead of towed streamer vessels for 4D surveys. In an OBN survey, autonomous seismic sensors are deployed on the seafloor for the duration of a campaign and then recovered; for repeat surveys they are accurately repositioned to reproduce the receiver geometry. This offers two key advantages for 4D: (1) the receiver geometry can be held constant with high accuracy, and (2) recording on the quiet seafloor reduces swell-related and sea-surface noise that affect towed-streamer data.

While geometric repeatability (source/receiver positions) is one aspect of 4D data quality, the marine environment itself presents another challenge: variations in the water column. Seawater is the first medium through which seismic waves travel in an active-source marine seismic survey, and its properties can change over time. The speed of sound in water (often called water velocity) depends on factors such as temperature, salinity, and pressure. As each of these properties increases, sound speed increases (Mackenzie, 1981). In practical terms, warmer or saltier water transmits sound faster, as does deeper water due to higher pressure.

Daily heating and cooling cycles, seasonal changes, ocean currents, internal tides, and other oceanographic phenomena can all perturb the water's temperature and salinity structure. Thus, the water sound-speed field can vary not only with depth, but also from place to place and over calendar time (Wang et al., 2012; Borges et al., 2022). For a one-off 3D

acquisition, modest water-velocity variations are usually a minor concern. They might slightly affect imaging but can often be handled by assuming an average water velocity during processing.

In a time-lapse context, however, even small changes in the water column between the baseline and monitor surveys can have an outsized impact on the seismic data. These timing differences can be on the order of a few milliseconds and are seemingly small, but highly significant for 4D seismic analyses. Such shifts are well within the limits of detectability of modern seismic, and if uncorrected they will appear as false anomalies when comparing baseline and monitor data. In fact, unrecognized water-column velocity variations can create the illusion of structural changes or amplitude differences in the subsurface, potentially leading to misinterpretation of geobodies like gas accumulations where there are none (Bertrand and MacBeth, 2005). In short, water velocity changes are a significant source of non-repeatability in marine 4D surveys (MacKay et al., 2003; Carvill, 2009; Wang et al., 2015). They contribute to the 4D noise floor and can mask the true reservoir signals if not properly handled. This has motivated the development of specialized approaches to measure and correct for water-velocity variations during 4D surveys (Osdal and Landrø, 2011; Ritter, 2010).

One straightforward approach to this problem is to perform direct measurements of water sound speed during the seismic surveys. For example, oceanographers and seismic crews use pressure-inverted echo sounders (PIES) and expendable probes to monitor water velocity and tide changes in real time (Wang et al., 2012). Other tools like CTD casts (conductivity-temperature-depth profilers) or SVPs (sound velocity profiles) from ship measurements provide snapshots of the vertical sound-speed profile at certain locations and times, which can be used to build or update the water-layer model. However, these measurements are inherently sparse and thus may miss spatial or temporal fluctuations that occur elsewhere or later.

Another approach is to extract water-column information from the seismic data itself.

The logic here is that the seismic recordings contain within them the imprint of the water layer, especially on certain parts of the wavefield like direct arrivals (the first arrivals that propagate through the water column from source to receiver) and water-bottom multiples (waves that bounce between the surface and seafloor). Since the travel time of these events directly depends on the water velocity, analyzing them can yield estimates of the water sound speed.

For OBN data, the seawater average velocity (SWAV) can be estimated from seismic measurements by exploiting differential times between the primary water-bottom multiple and the first arrival, or by tomographic inversion of water-bottom traveltimes. Both approaches have been demonstrated in field settings (Lacombe et al., 2006; Ritter, 2010; Li et al., 2016). Small but detectable SWAV variations of typically a few meters per second have been reported and shown to introduce millisecond-scale time shifts relevant for 4D repeatability (MacKay et al., 2003; Li et al., 2016).

One limitation of earlier approaches cited in the literature, however, is that they assume horizontally uniform water velocity, only varying with depth or over time in a bulk sense (Amini et al., 2016). In other words, the water layer is treated as a 1D column or a layer with one average velocity at a given time. This simplification means lateral gradients or local anomalies in water sound speed cannot be resolved by those methods. In reality, as discussed above, there can be significant lateral variations—for example, one side of a survey area might have slightly warmer surface waters than the other due to currents, leading to different velocities. Ignoring such lateral changes can leave residual timing errors in the data.

The goal of this thesis is to address the water-velocity variation problem in time-lapse seismic by estimating a time-dependent water velocity model directly from seismic data, with sufficient resolution in both space and time. We develop a tomographic inversion methodology that explicitly models the water sound speed as a function of space (lateral and vertical) and of calendar time. By employing regularization in both the spatial

and time domains, this is achieved without imposing structural limitations on the velocity field.

The remainder of this document is organized as follows: Chapter 2 presents the detailed methodology and theory of our time-dependent water velocity inversion (along with a literature review of related methods) and then applies the approach to controlled synthetic examples and discusses the results. Chapter 3 draws conclusions and outlines recommendations for applying this work to real field data and extending it in future research.

CHAPTER 2

TIME-DEPENDENT WATER VELOCITY INVERSION FROM OBN SEISMIC DATA

Tiago Cabral[1,2,3,4], Paul Sava[4]

2.1 Abstract

Variations in water-column seismic velocity are a dominant source of time-lapse (4D) noise in deep-water ocean-bottom-node (OBN) surveys, degrading repeatability and obscuring subtle reservoir changes. We present a traveltime-tomography method that estimates a spatiotemporal water-column velocity model from OBN first arrivals for 4D processing. Traveltimes are modeled with a straight-ray approximation valid for small velocity contrasts and moderate offsets, and we invert for water sound speed on a regular grid in space and calendar time. We minimize traveltime misfit with joint spatial and calendar-time smoothness, plus a depth-aware pull-to-reference that encodes expected variability with depth. We solve the system matrix-free with preconditioned conjugate gradients, enabling large problems without forming normal matrices. Two synthetic studies—a moving Gaussian anomaly and a deep-water, field-inspired scenario concentrated in the upper ocean—demonstrate markedly improved 4D repeatability: temporal regularization suppresses pick-noise artifacts, and depth-aware weights confine updates to the upper ocean and reduce vertical smearing, yielding cleaner reverse-time migration (RTM) difference images than spatial-only or spatially homogeneous time-varying water models. The formulation and results motivate extensions to 3D geometry, joint estimation of source/receiver positioning errors, and direct assimilation of oceanographic measurements.

[1]Primary research and author.
[2]Author for correspondence. Email: tiago_cabral@mines.edu.
[3]Petrobras, Rio de Janeiro, Brazil.
[4]Center for Wave Phenomena, Colorado School of Mines, Golden, Colorado, United States of America.

2.2 Introduction

Time-lapse (4D) seismic surveys acquire multiple datasets over the same area at different times; differences computed after cross-equalization (amplitude/phase matching and, where appropriate, static/warping corrections) highlight temporal changes relative to a baseline image (Johnston, 2013; Romero et al., 2022). These surveys are widely used to monitor subsurface changes and manage hydrocarbon reservoirs by tracking fluid movement during production and injection (Johnston, 2013; Mitra, 2023). However, the fidelity of a 4D image is highly sensitive to the repeatability of acquisition geometry and environmental conditions between surveys (Borges et al., 2022). Achieving high-quality 4D results is particularly challenging in carbonate reservoirs, where the stiff rock frame yields a weaker seismic response to saturation or pressure perturbations than in more compliant clastics (Jervis et al., 2018). As a result, even well-processed 4D signals can be extremely subtle in carbonates, increasing the risk that nonrepeatable noise overwhelms the true reservoir response. To improve repeatability offshore, ocean-bottom-node (OBN) acquisitions are increasingly employed: fixed or accurately redeployed seabed receivers provide more consistent geometry and are less susceptible to sea-surface noise than towed streamers (Kiyashchenko et al., 2020; Zhang et al., 2021).

A major contributor to 4D noise is variability in water-column sound speed (water velocity). In a single, 3D survey, the water-column model is often treated as laterally uniform and only mildly depth dependent, with minimal impact on that final seismic image. In a time-lapse setting, by contrast, small spatial or temporal changes in sound speed between vintages produce measurable traveltime shifts of direct and reflected arrivals, which in turn create spurious differences in the 4D image if left uncorrected (MacKay et al., 2003; Wang et al., 2013). The magnitude of these shifts scales with the two-way water path length, so deeper water amplifies timing errors. Oceanic sound speed depends primarily on temperature, salinity, and pressure: it increases with warmer temperature, higher salinity, and greater pressure (Mackenzie, 1981; IOC et al., 2010). Typical deep-water

values are on the order of 1480–1550 m/s. Because temperature generally decreases with depth in the upper ocean while pressure increases, the vertical profile of sound speed can be nonmonotonic (Figure 2.1). Vertical variations are routinely measured with sound-velocity profilers (SVPs), but lateral and temporal variations—driven by seasonal heating/cooling, internal tides and fronts, currents, and tide-induced water-level changes—are harder to predict and sample adequately (Wang et al., 2013; Hatchell et al., 2019). Figure 2.2 (page 9) shows example SVP measurements depicting water velocity variation occurring over the duration of the OBN survey. In these examples, for a given location and depth, the variations rarely exceed ±10 m/s (≈ ±0.7%) from the mean profile. They are predominant in the first 1 km of water depth, but otherwise do not seem to exhibit a predictable pattern. As a complement to sparse SVP casts, inverting first-arrival traveltimes can recover the water-layer velocity field at survey scale and cadence, providing a more complete, dynamically updated picture (Ritter, 2010; Udengaard and Craft, 2012).

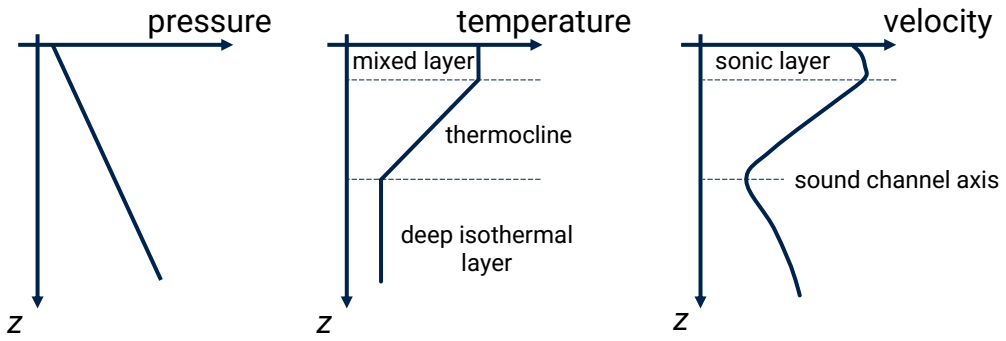

Figure 2.1: Idealized profiles of physical properties in the ocean water layer vs. depth, showing (left) increasing pressure, (middle) decreasing temperature in the thermocline, and (right) resulting non-monotonic acoustic velocity.

Despite the importance of correcting for water-column variability, many previous inversion workflows treat the water layer as static or overly simplified. For example, Muijzert et al. (2022) perform a joint inversion of direct-arrival times to refine OBN acquisition parameters (including water velocity, source positions, node positions, and timing), but assume a time-invariant water-velocity model for each survey vintage. Amini et al. (2016) extend earlier efforts by jointly inverting for water velocity and receiver-node positions in

OBN data; however, their methodology still imposes a spatially uniform water speed at each acquisition time (an average value per vintage), rather than resolving lateral gradients or temporal evolution between surveys. These limitations motivate approaches that explicitly handle both spatial and time-varying water-velocity structure in a time-lapse context.

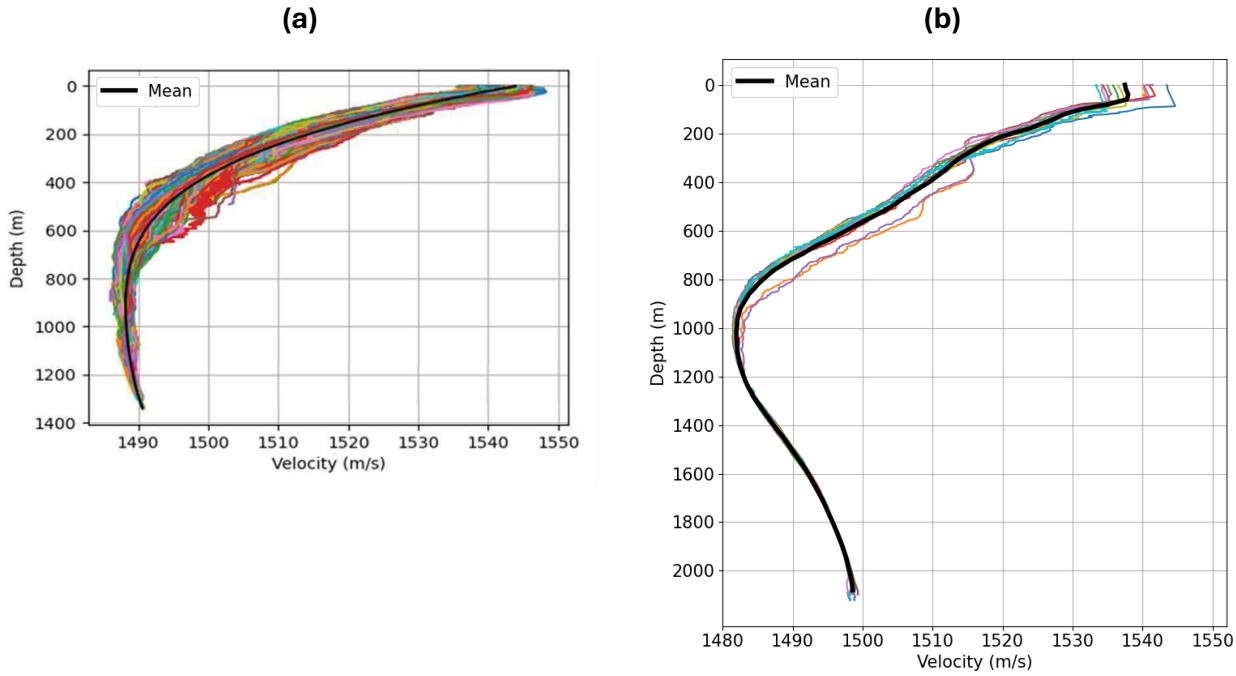

Figure 2.2: Water-layer acoustic velocity profiles acquired during field OBN surveys: (a) from the north-central part of the Green Canyon Protraction Area in the Gulf of Mexico (Seymour et al., 2021); (b) from the Tupi field in Brazil. The colored curves represent individual profiles at different locations and times, while the black curve shows the average profile.

Here, we develop and test a traveltime tomographic inversion that parameterizes the water-layer velocity field as a function of space $\mathbf{x}$ and calendar time T. Using synthetic OBN seismic data, we minimize a misfit to first-arrival picks with joint regularization in the spatial $\mathbf{x}$ dimensions and along the temporal axis T. This spatio-temporal regularization stabilizes the inversion and encourages smoothly varying velocity models in both space and time. We demonstrate that the method can recover time-dependent water-velocity anomalies even with limited source–receiver offsets typical of first-break tomography. We

show that incorporating temporal smoothness is crucial for distinguishing true velocity changes from random picking errors or sparse coverage effects. Accurate time-lapse water-velocity models, in turn, can significantly improve 4D repeatability by removing water-column-related traveltime noise and clarifying genuine reservoir signals.

2.3 Theory

We model the calendar-time–dependent water velocity as $v(\mathbf{x}, T)$, where $\mathbf{x} = (x, y, z)$ and T denotes survey (calendar) time. The unknown quantity we invert for is the slowness $s(\mathbf{x}, T) = 1/v(\mathbf{x}, T)$. The data are first-arrival (direct-water) traveltimes $\mathbf{t}^{\text{obs}}$ measured between known source and receiver positions in an ocean-bottom-node (OBN) acquisition. We discretize $(\mathbf{x}, T)$ on a regular grid and group all slowness samples into a parameter vector $\mathbf{s}$.

2.3.1 Problem Setup and Intuition

Our goal is to estimate $v(\mathbf{x}, T)$ (equivalently $s(\mathbf{x}, T)$) that may vary over space and calendar time. We use uppercase T for survey time and lowercase t for physical wave propagation traveltime. In OBN surveys, sources are near the sea surface and receivers on the seafloor; the direct arrival propagates within the water column and, for a single shot record, the medium can be assumed quasi-static, with no appreciable change in s during that record.

For a source at $\mathbf{x}_S$ and receiver at $\mathbf{x}_R$, the predicted direct-arrival time at survey time index T_k is the path integral of slowness along the propagation path γ_{SR}:

$$t_{SR}(T_k) = \int_{\gamma_{SR}} s(\mathbf{x}, T_k)\, \mathrm{d}\ell. \tag{2.1}$$

Two practical considerations apply. (i) Reliable picking is limited to pre-critical incidence at the seafloor; at larger grazing angles the water-bottom head wave and shallow-path re-

flections can precede or interfere with the direct water arrival, and phase reversals may occur. (ii) Although γ_{SR} is, in principle, curved by lateral velocity variations (Snell's law), water-column contrasts are typically smaller than 50 m/s on a $\sim$ 1500 m/s background, so the straight-ray approximation is adequate in many practical settings (Muijzert et al., 2022). We therefore approximate γ_{SR} by the straight segment between $\mathbf{x}_S$ and $\mathbf{x}_R$ within the water layer.

Let the spatial domain be partitioned into n_{cell} voxels and the survey time into n_T slices. Spatial sampling reflects the expected resolution and computational constraints, and time sampling reflects how fast the water velocity changes relative to acquisition cadence. In practice, assuming piecewise-constant $s(\cdot, T)$ per sail line is a reasonable starting point (Xu and Pham, 2003).

Approximating equation (2.1) by a Riemann sum yields

$$t_{SR}(T_k) \;\approx\; \sum_{j=1}^{n_{\text{cell}}} g_{SR,j}\; s_j(T_k), \tag{2.2}$$

where $g_{SR,j}$ is the length of the straight segment γ_{SR} inside voxel j. All reliable picks at T_k collectively give

$$\mathbf{t}_k \;\approx\; \mathbf{G}_k\, \mathbf{s}_k, \tag{2.3}$$

with sparse path-length matrix $\mathbf{G}_k \in \mathbb{R}^{n_{\text{data}}(k)\times n_{\text{cell}}}$ and $\mathbf{s}_k \in \mathbb{R}^{n_{\text{cell}}}$. Stacking all time slices leads to

$$\mathbf{t} \;=\; \begin{bmatrix} \mathbf{t}_1 \\ \mathbf{t}_2 \\ \vdots \\ \mathbf{t}_{n_T} \end{bmatrix} \;\approx\; \underbrace{\operatorname{diag}\big(\mathbf{G}_1, \mathbf{G}_2, \ldots, \mathbf{G}_{n_T}\big)}_{\mathbf{G}} \begin{bmatrix} \mathbf{s}_1 \\ \mathbf{s}_2 \\ \vdots \\ \mathbf{s}_{n_T} \end{bmatrix} \;=\; \mathbf{G}\,\mathbf{s}. \tag{2.4}$$

2.3.2 Inverse Problem Formulation

We estimate $\mathbf{s}$ by minimizing a Tikhonov-regularized objective that enforces data fit and smoothness in space and calendar time, with an optional depth-weighted pull toward

a reference model $\mathbf{s}_0$:

$$\mathcal{J}(\mathbf{s}) = \underbrace{\|\mathbf{G}\mathbf{s} - \mathbf{t}^{\text{obs}}\|_2^2}_{\mathcal{J}_d} + \alpha \underbrace{\|\mathbf{\Gamma}_{\mathbf{x}}\mathbf{s}\|_2^2}_{\mathcal{J}_{\mathbf{x}}} + \beta \underbrace{\|\mathbf{\Gamma}_T\mathbf{s}\|_2^2}_{\mathcal{J}_T} + \underbrace{\|\mathbf{W}(\mathbf{s} - \mathbf{s}_0)\|_2^2}_{\mathcal{J}_W}, \tag{2.5}$$

where $\mathbf{\Gamma}_{\mathbf{x}}$ is a first-order spatial finite-difference *gradient* operator (applied per time slice), $\mathbf{\Gamma}_T$ is a first-order finite difference along calendar time (applied per spatial location), $\alpha, \beta \geq 0$ tune spatial and temporal smoothing, and $\mathbf{W} = \text{diag}(w_1, \ldots, w_{n_{\text{par}}})$ encodes spatially varying trust in $\mathbf{s}_0$. Large w_i anchor parameters (e.g., deeper water where variability is minimal), while small w_i permit deviation. We initialize the depth profile with $w_i \in [0, 1]$ (relative weights) and, during tuning, apply a single uniform rescaling to all diagonal entries to set the global strength of $\mathcal{J}_W$; this global factor is absorbed into $\mathbf{W}$, so no separate multiplier appears in the equation.

The associated normal equations are

$$\left(\mathbf{G}^\top\mathbf{G} + \alpha\,\mathbf{\Gamma}_{\mathbf{x}}^\top\mathbf{\Gamma}_{\mathbf{x}} + \beta\,\mathbf{\Gamma}_T^\top\mathbf{\Gamma}_T + \mathbf{D}\right)\mathbf{s} \;=\; \mathbf{G}^\top\mathbf{t}^{\text{obs}} \;+\; \mathbf{D}\,\mathbf{s}_0, \tag{2.6}$$

where $\mathbf{D} = \mathbf{W}^\top\mathbf{W} = \text{diag}(w_1^2, \ldots, w_{n_{\text{par}}}^2)$.

2.3.3 Numerical Solution of the Regularized Normal Equations

The coefficient matrix in equation (2.6) is symmetric positive definite (SPD) provided the combined action of data coverage and regularization removes nullspaces, which is typically the case in practice. We solve equation (2.6) with preconditioned Conjugate Gradients (PCG), exploiting the SPD matrix structure. Warm-starting with $\mathbf{s}^{(0)} = \mathbf{s}_0$ reduces iterations. We terminate when the relative residual satisfies

$$\frac{\|\mathbf{b} - \mathbf{A}\mathbf{s}^{(k)}\|_2}{\|\mathbf{b}\|_2} \leq 10^{-6}, \tag{2.7}$$

where $\mathbf{A}$ and $\mathbf{b}$ are the normal operator and right-hand side in (2.6). This tolerance is dimensionless.

We avoid forming $\mathbf{G}^\top\mathbf{G}$ due to memory constraints. A matrix-free linear operator implements

$$\mathbf{v} \mapsto \mathbf{G}^\top(\mathbf{G}\mathbf{v}) + \alpha\,\mathbf{\Gamma}_{\mathbf{x}}^\top(\mathbf{\Gamma}_{\mathbf{x}}\mathbf{v}) + \beta\,\mathbf{\Gamma}_T^\top(\mathbf{\Gamma}_T\mathbf{v}) + \mathbf{D}\,\mathbf{v}. \tag{2.8}$$

We select the regularization weights with an L-curve analysis (Hansen and O'Leary, 1993; Hansen, 2010). First, with $\beta = 0$, we sweep α on a logarithmic grid and choose the corner of the curve $\big(\|\mathbf{G}\mathbf{s} - \mathbf{t}^{\text{obs}}\|_2,\ \|\mathbf{\Gamma}_{\mathbf{x}}\mathbf{s}\|_2\big)$. We then fix that α and sweep β, using $\big(\|\mathbf{G}\mathbf{s} - \mathbf{t}^{\text{obs}}\|_2,\ \|\mathbf{\Gamma}_T\mathbf{s}\|_2\big)$. In our numerical examples, single passes for α and β were sufficient. To reduce cost, the L-curve can be built on a representative subset of traveltime picks; we found this yields essentially the same α, β.

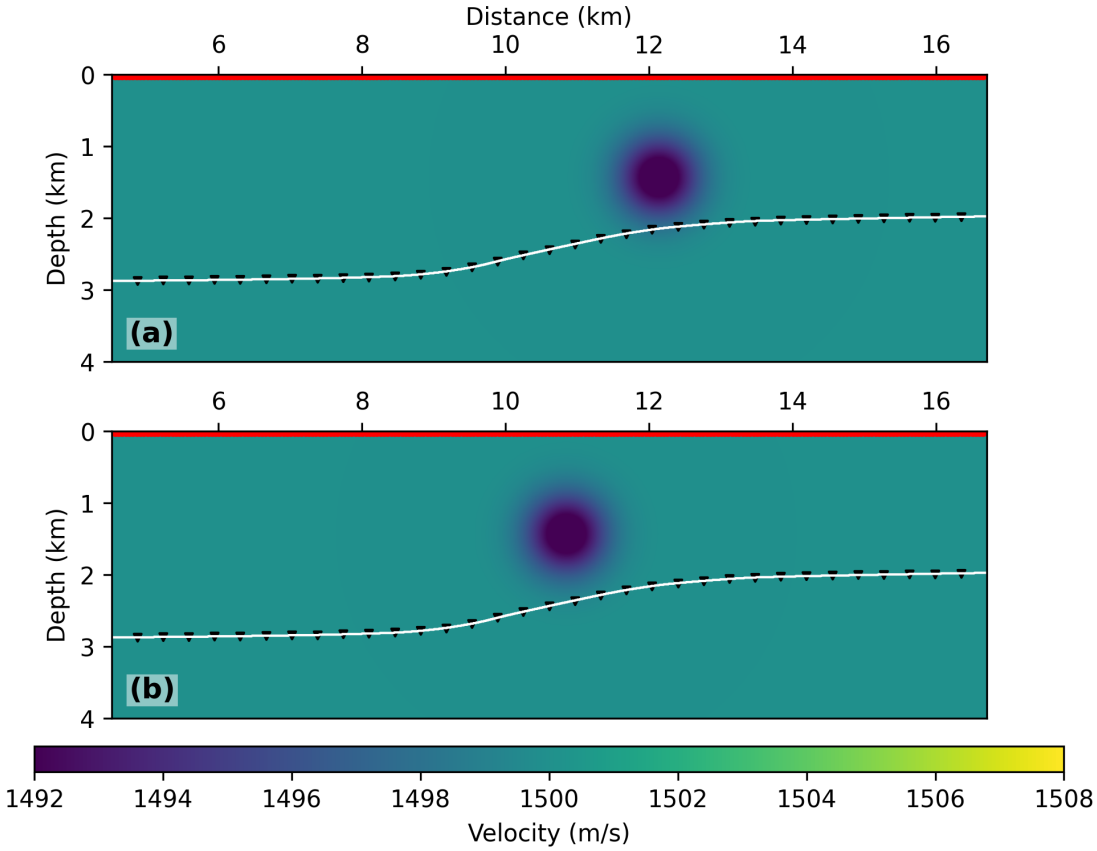

Figure 2.3: Gaussian water-layer model used in the first experiment at calendar times: (a) 0 days and (b) 12 days.

2.4 Numerical Examples

We assess the proposed approach using two-dimensional (2D) synthetic experiments. To make the tests geologically plausible, water-velocity statistics and temporal trends observed in field measurements from the Santos Basin (Brazil) were used to inform the synthetic models. We consider two scenarios: (i) a translating Gaussian anomaly and (ii) a more realistic, horizontally varying velocity field.

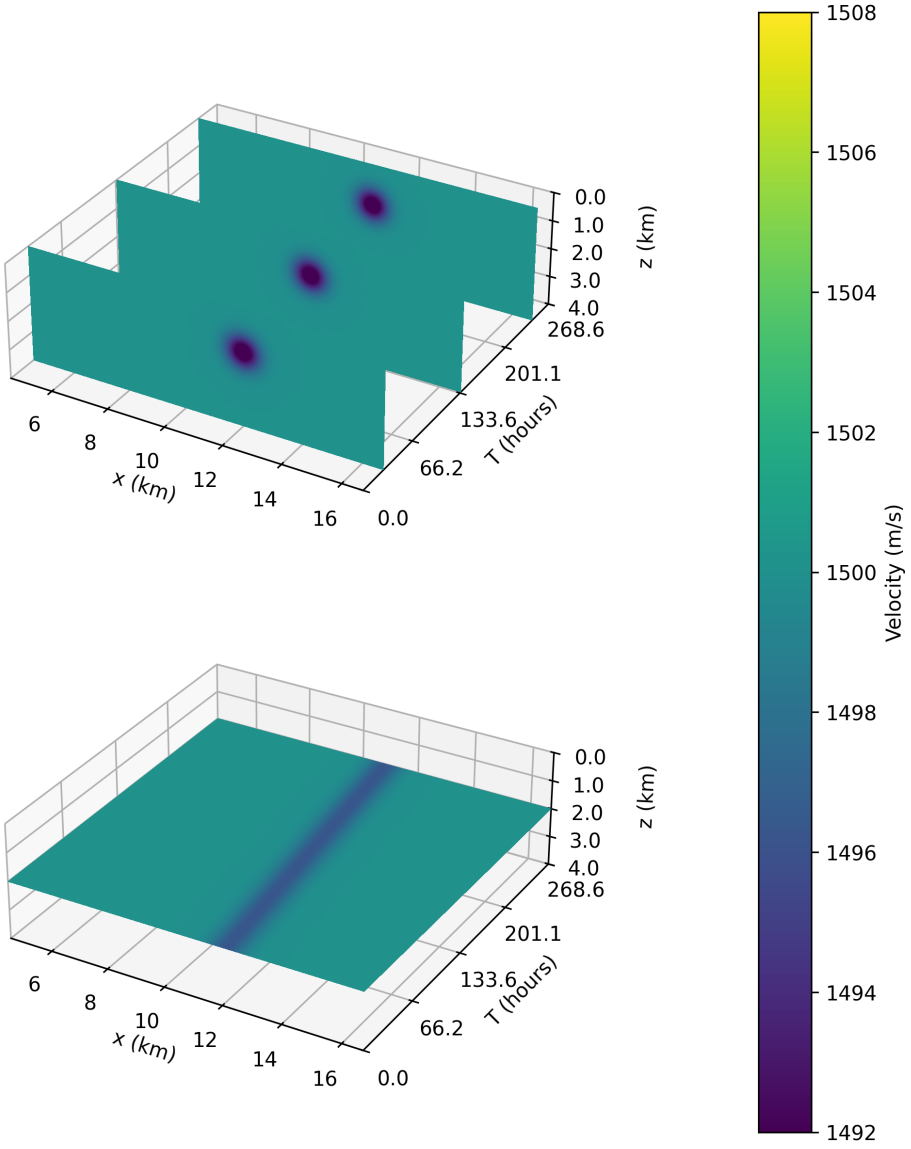

Figure 2.4: 3D representation of the Gaussian model. On the top, slices at $T = 1.1$ days, $T = 5.6$ days, $T = 10.1$ days. On the bottom, slice at depth $z = 2$ km.

2.4.1 Gaussian Anomaly

The first experiment consists of a negative Gaussian anomaly of amplitude -10 m/s and standard deviation 400 m, translating to the left (negative x-direction) at 4.8 m/h within a water layer whose depth varies between 2000 and 3000 m. The model is discretized on a uniform $x - z$ grid with $\Delta x = \Delta z = 7.62$ m. While intentionally idealized, this setup highlights the algorithm's ability to recover an anomaly's shape, magnitude, and location. Figure 2.3 (page 13) displays the true model at the initial and final survey times. Figure 2.4 (page 14) shows a slice of that same model to illustrate its 3D structure.

The acquisition emulates an OBN survey with 200 sail lines separated by 80 minutes, which is the same interval between samples in the survey-time axis. Source spacing is 50 m and receiver spacing is 360 m. Picked traveltimes were perturbed with zero-mean Gaussian noise of standard deviation 1.5 ms to emulate uncertainties associated with source/receiver positioning, deconvolution, and other measurement errors. This level of noise is consistent with ~ 2 m combined uncertainty in vertical positioning for typical water sound speeds.

Inversions are performed on a uniform grid with $\Delta x = \Delta z = 152.4$ m. The true model is interpolated to this grid for comparison. Two baseline inversions use only spatial smoothness regularization: one with noise-free traveltimes (Figure 2.5b, page 16) and one with noisy traveltimes (Figure 2.5c). Compared to the true model (Figure 2.5a), the noisy case exhibits pronounced artifacts, indicating high sensitivity to traveltime noise when only spatial regularization is applied. This behavior is expected given the relatively small velocity contrasts being targeted ($|\Delta v|<10$ m/s).

A third inversion adds calendar-time regularization while using the same noisy traveltimes (Figure 2.5d). Incorporating temporal smoothness reduces artifact energy away from the anomaly, and the recovered feature more closely resembles the clean-data inversion. In all recovered models the anomaly is somewhat smeared, particularly in the vertical direction, reflecting the limited horizontal illumination of the acquisition. Additionally, smooth-

ness across the water bottom causes the recovered anomaly to "bleed" into the subsurface; in practice, this is easily mitigated by replacing velocities below the mapped water bottom with migration velocities.

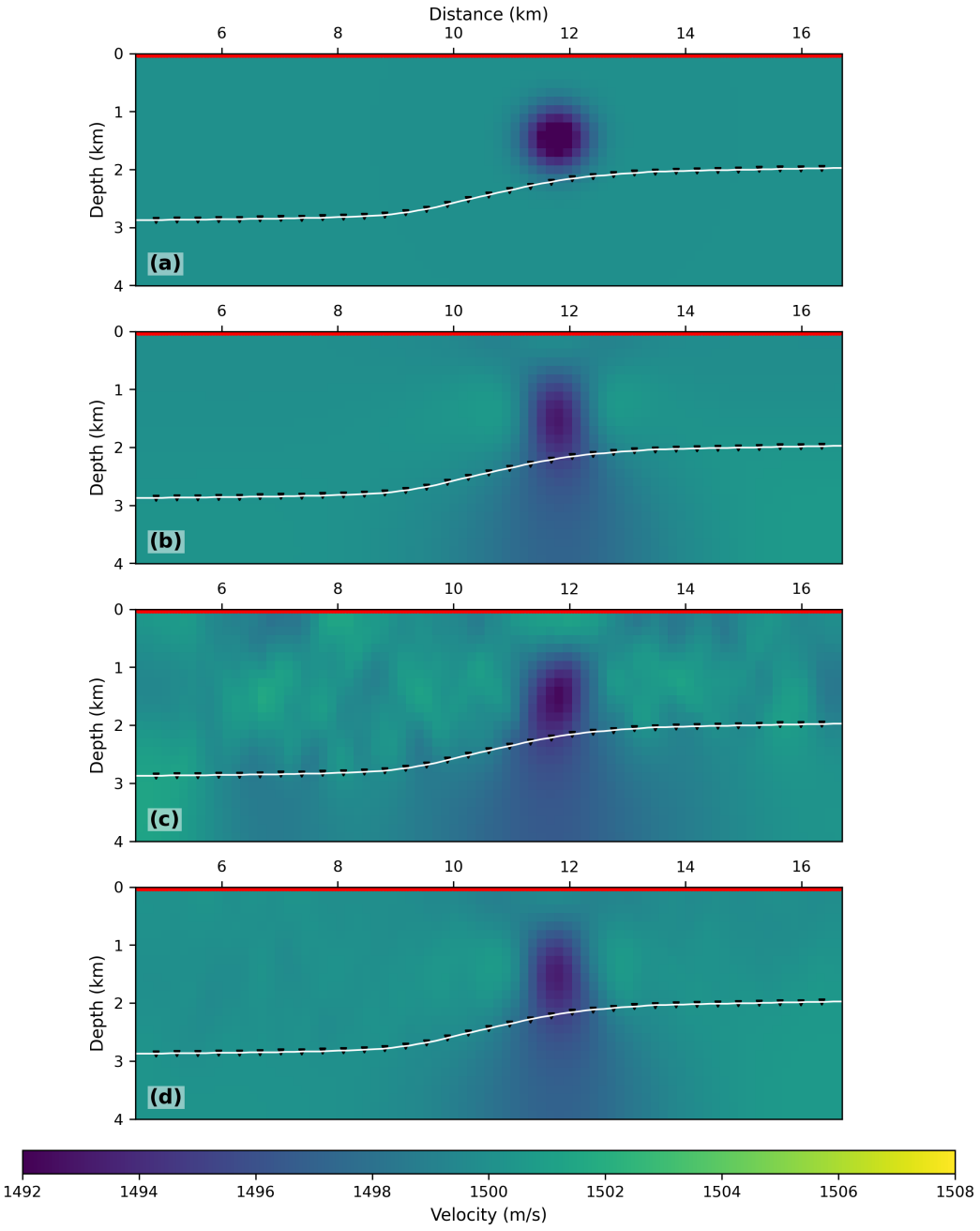

Figure 2.5: Inversion results for the Gaussian-anomaly experiment at $T \approx 3$ days. (a) True model regridded onto the inversion grid. (b) Spatial-regularization only, clean traveltimes. (c) Spatial-regularization only, noisy traveltimes. (d) Spatial + calendar-time regularization, noisy traveltimes. The white line denotes the water bottom.

2.4.2 Realistic Water Variation

The second experiment prescribes a horizontally varying, time-dependent water layer inspired by data from the Santos Basin, Brazil (Figure 2.6). The model superposes two sinusoidal components of wavelength 48 km and 24 km along x, confined to depths shallower than 800 m to mimic the stronger near-surface variability observed in the measurements.

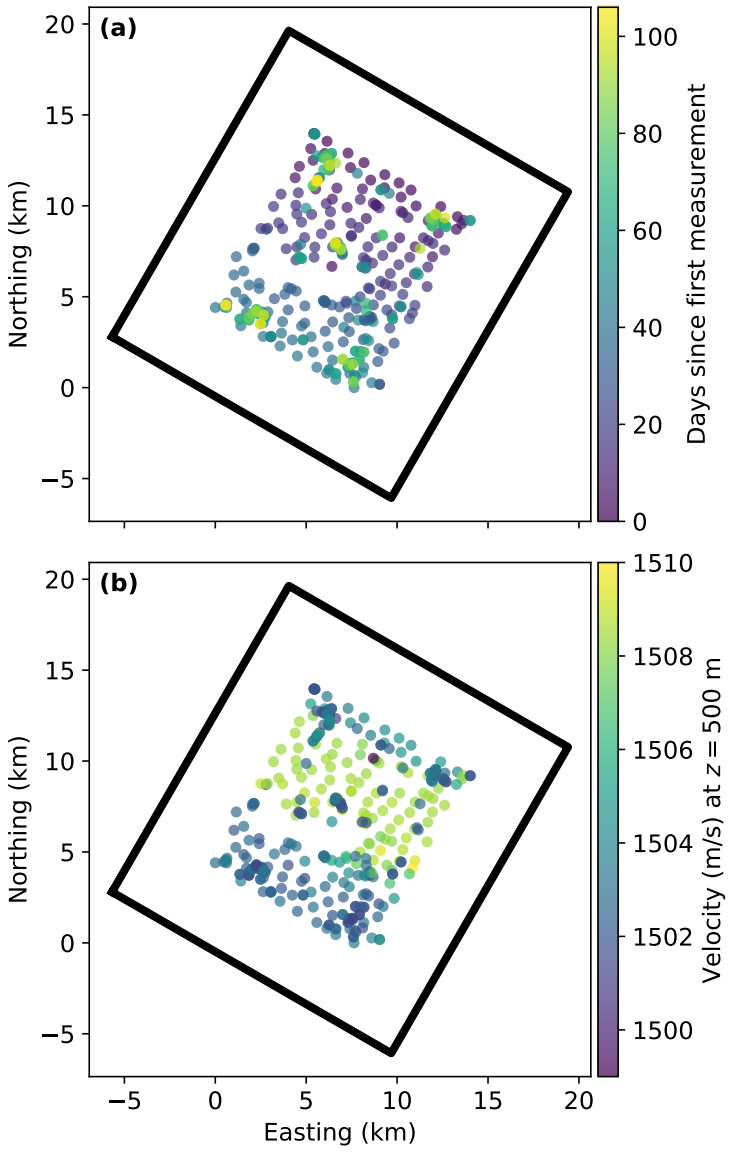

Figure 2.6: Locations of discrete seismic velocity profiles measured during an OBN acquisition in the Santos Basin, Brazil: (a) colored by acquisition time and (b) colored by velocity value at depth 500 m.

The inversion grid and acquisition parameters match those of the first experiment. We test two regularization strategies: (i) joint spatial and calendar-time smoothness, and (ii) the same regularization plus spatially varying weights that down-weight updates at depth. Specifically, the data-term weights are set to unity for depths smaller than 750 m, linearly increase between 750 and 1250 m, and reach 1000 at depths larger than 1250 m. This choice encodes prior knowledge that water-velocity variations are predominantly shallow. The reference model $\mathbf{s}_0$ is a spatially homogeneous water velocity of 1500 m/s at all times.

Figure 2.7 (page 19) compares the true and inverted water layers at $T \approx 3$ days. Both inversions recover the large-scale left-to-right velocity trend. However, limited illumination causes substantial vertical smearing when no depth-weighting is used. Introducing the weights confines updates to likely depths, suppresses spurious deep structure, and visibly reduces vertical smearing. Figure 2.8 (page 20) shows a 3D representation of the inverted result where varying depth weights were used.

To evaluate the impact on time-lapse imaging, we combined each inverted water layer with deeper portions from a cropped version of the Sigsbee model (Paffenholz et al., 2002; Bishop, 2003), depicted in Figure 2.9 (page 21) to build full velocity models for reverse-time migration (RTM). Two-dimensional synthetic data were generated with the true model using a finite-difference acoustic solver. A Ricker wavelet with peak frequency 25 Hz was used for modeling. After removing direct arrivals, the data were migrated with (i) the true model and (ii) each inverted model. Post-migration, a mild Laplacian filter was applied to attenuate migration noise, and images were muted above the water bottom. The image obtained using the true water-layer model was treated as a reference for comparison against the images obtained from the inverted models. The difference images (inverted minus reference) quantify residual artifacts caused by water-velocity errors (Figure 2.10, page 22, and Figure 2.11, page 23).

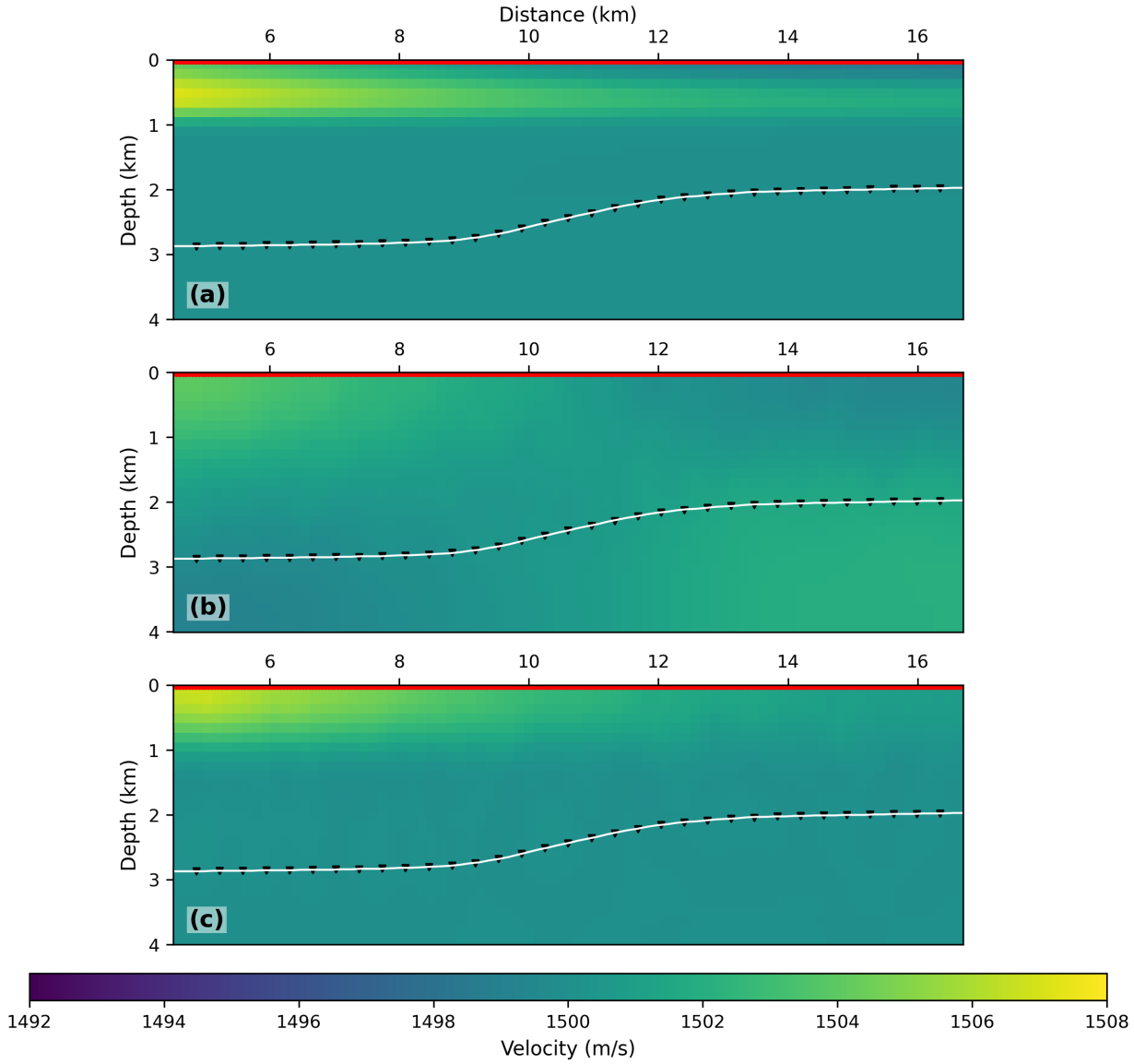

Figure 2.7: Inversion results for the realistic water-velocity scenario at $T \approx 3$ days. (a) True model regridded to the inversion grid. (b) Spatial + calendar-time regularization (no depth weights). (c) Same regularization with spatially varying depth weights that favor updates above $\sim$1 km. The white line denotes the water bottom.

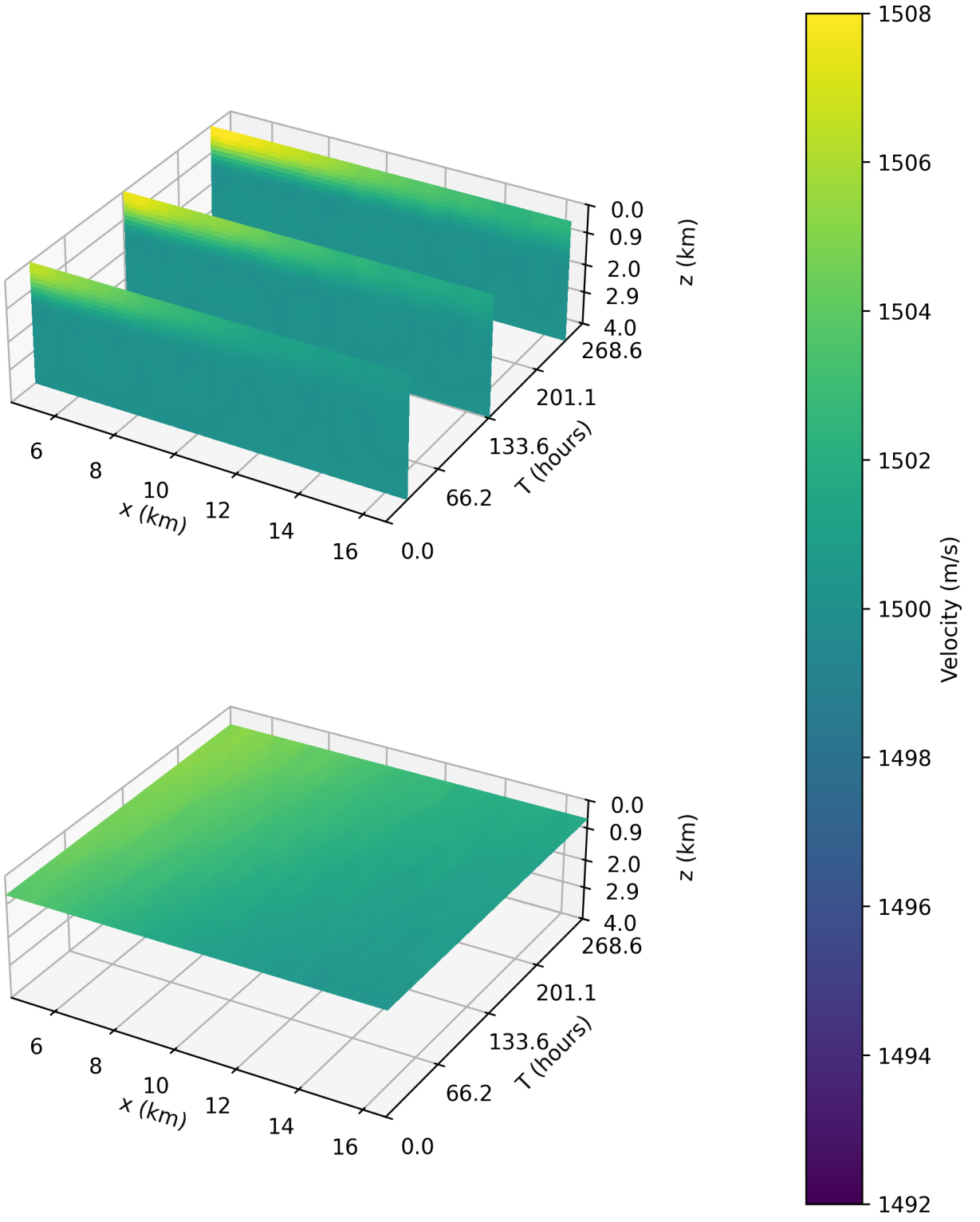

Figure 2.8: 3D representation of the inverted result from the realistic water-velocity scenario where varying depth weights were used. On the top, slices at $T = 1.1$ days, $T = 5.6$ days, $T = 10.1$ days. On the bottom, slice at depth $z = 600$ m.

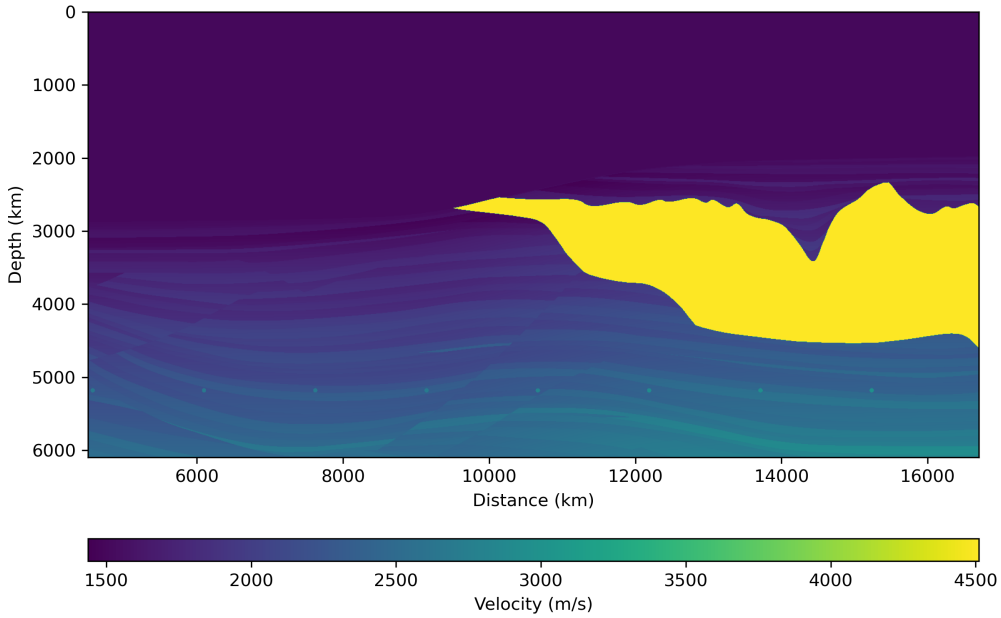

Figure 2.9: Sigsbee velocity model used for the imaging experiments.

Depth-weighted inversion yields visibly fewer artifacts than the unweighted case (compare Figure 2.10b and Figure 2.10c). In both cases, residuals are larger at shallow depths, consistent with steeper ray paths sampling shallower reflectors and thus caused increased sensitivity to vertical smearing. A third test with a spatially homogeneous (but time-varying) water velocity (Figure 2.10a) performs worst, showing stronger artifacts compared to spatially varying solutions.

For each difference image, we computed a normalized RMS (NRMS) measure between 3 and 4 km depth,

$$\text{NRMS} = \frac{2\ \text{RMS}\big(\mathbf{i} - \mathbf{i}_{\text{ref}}\big)}{\text{RMS}(\mathbf{i}) + \text{RMS}\big(\mathbf{i}_{\text{ref}}\big)}\,, \tag{2.9}$$

where $\mathbf{i}$ is the image produced with an inverted model and $\mathbf{i}_{\text{ref}}$ is the image obtained with the true (reference) model. The NRMS values obtained were: 8.5% for the homogeneous water layer inversion, 0.61% for the inversion without depth weights, and 0.28% for the inversion with depth weights. Since lower NRMS values indicate a smaller difference, and therefore better inversion performance, these NRMS results corroborate the qualitative analysis of the images in Figure 2.10.

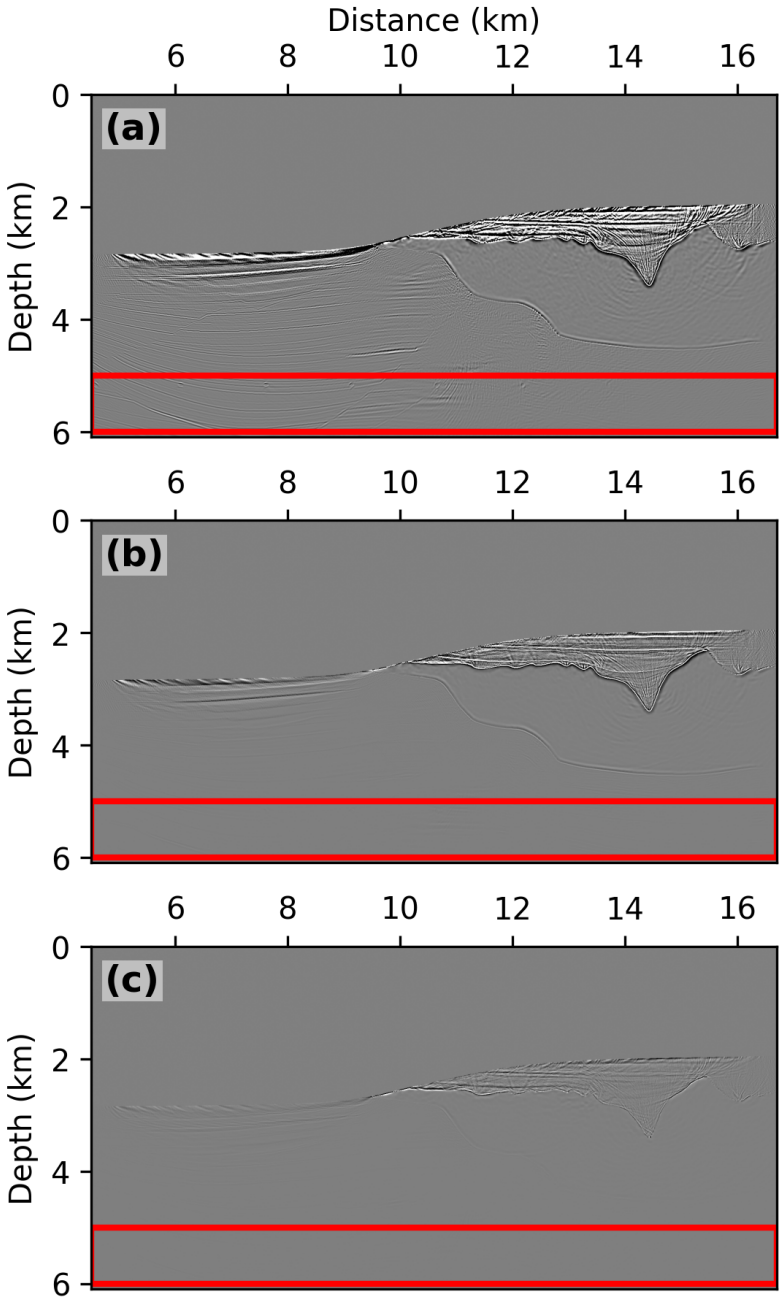

Figure 2.10: RTM difference images (inverted minus reference) using water layers from: (a) a spatially homogeneous but time-varying water velocity, (b) inversion without depth weights, and (c) inversion with shallow-favoring depth weights. The red box highlights the region of interest where the NRMS metric is computed.

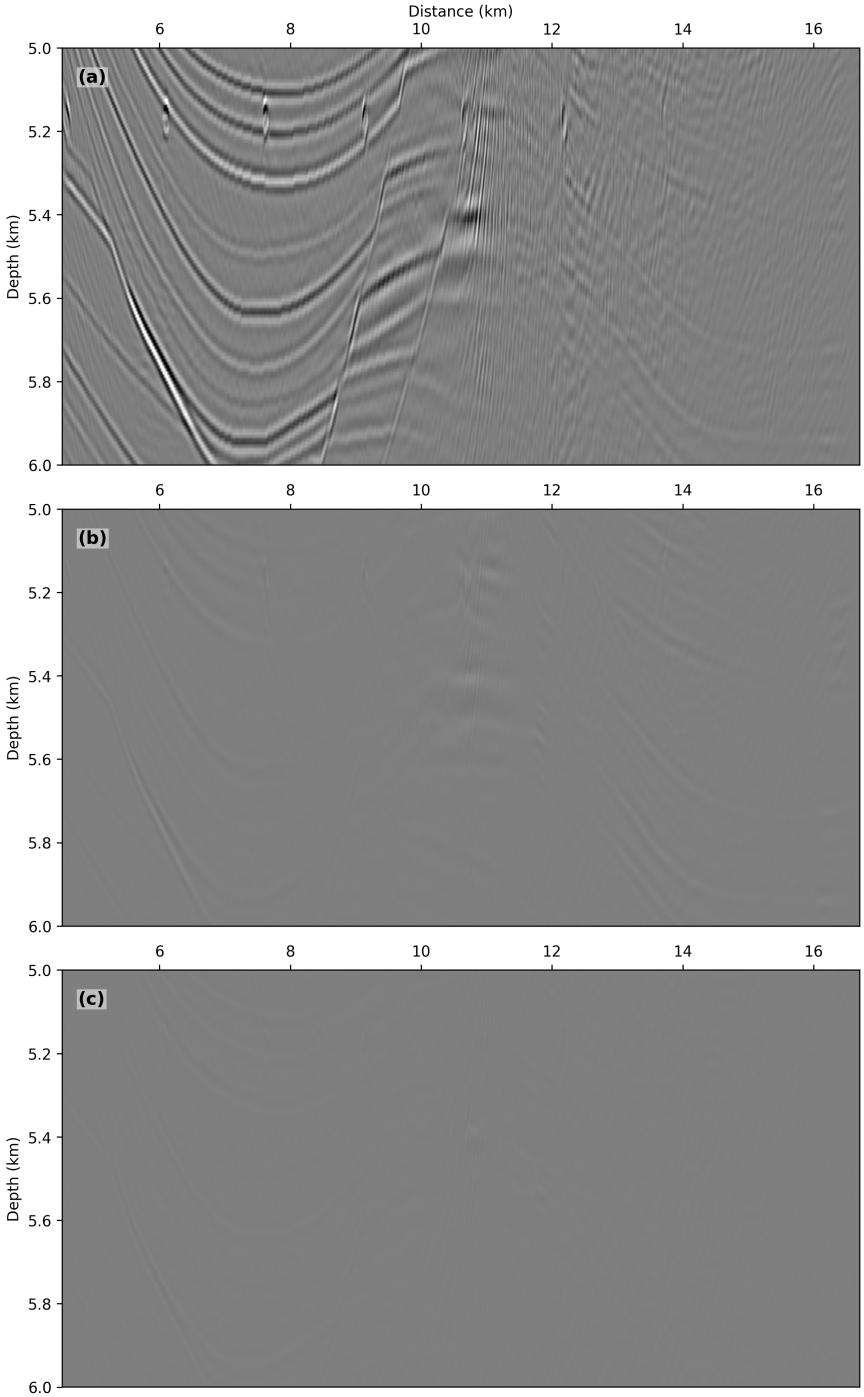

Figure 2.11: RTM difference images (inverted minus reference), zoomed into the region of interest where the NRMS metric is computed. The water layers used for migration are: (a) a spatially homogeneous but time-varying water velocity, (b) inversion without depth weights, and (c) inversion with shallow-favoring depth weights.

2.5 Discussion

Allowing the water velocity to vary in both space and calendar time leads to a high-dimensional inverse problem that is ill-posed without regularization. The Gaussian-anomaly experiment demonstrates strong sensitivity to traveltime noise when only spatial smoothness is used; adding calendar-time regularization effectively suppresses noise-induced artifacts for noise levels on the order of 1.5 ms, which is consistent with typical OBN acquisition uncertainties.

Incorporating spatially varying depth weights encodes practical prior knowledge: water-layer velocity variations are predominantly shallow. These weights restrict updates at depth, reduce vertical smearing, and improve 4D imaging outcomes, as corroborated by lower NRMS and cleaner RTM difference images.

All tests shown here are 2D; extension to 3D will introduce sparser, less repeatable illumination and substantially higher computational cost, which may increase the reliance on temporal regularization (and informative weighting) to maintain stability. Additionally, we did not jointly estimate source/receiver positions, which are commonly included in field workflows; adding joint inversion for positioning errors alongside water velocity would make the approach more realistic and allow a controlled assessment of trade-offs between model complexity, stability, and 4D image quality. Future work will address these aspects and apply the method to field data.

2.6 Conclusions

In this study we introduced a spatio-temporal traveltime tomography for the water layer in OBN 4D, parameterized as $v(\mathbf{x}, T)$, and stabilized with spatial and calendar-time regularization plus depth-dependent weighting. Synthetic experiments (a translating Gaussian anomaly and a data-informed "realistic" case) show that temporal regularization is essential to suppress the high sensitivity of first-arrival tomography to pick noise on the order of 1–2 ms, while shallow-focused weighting helps confine updates where variability

is expected and reduces vertical smearing. When used for migration, models produced by the proposed inversion reduce 4D difference artifacts and NRMS relative to (i) spatial-only regularization and (ii) time-varying but spatially homogeneous water-velocity updates, indicating a tangible improvement in 4D repeatability.

The current study used straight-ray paths, repeated geometry, and a 2D approximation for efficiency; extending to 3D OBN and jointly handling source and receiver positioning uncertainties are natural next steps. Future work will integrate SVP-derived priors and uncertainty into the weighting and validate the workflow on field OBN datasets to quantify repeatability gains.

2.7 Acknowledgements

The first author thanks Petrobras for the sponsorship that made this research possible. We thank the sponsors of the Center for Wave Phenomena at the Colorado School of Mines.

CHAPTER 3

SUMMARY AND FUTURE DIRECTIONS

This thesis presents a tomographic inversion framework for recovering time-varying water-column velocity fields from ocean-bottom node seismic data. By parameterizing the water velocity as a function of both spatial coordinates and calendar time, the method addresses a critical challenge in time-lapse seismic processing: the contamination of 4D signals by water-layer variations. The approach minimizes a misfit between observed and predicted first-arrival traveltimes while incorporating joint regularization across spatial and temporal dimensions, effectively stabilizing an otherwise ill-posed inverse problem.

The numerical experiments on synthetic data demonstrate that temporal regularization is essential for distinguishing true velocity changes from artifacts induced by measurement noise and sparse coverage. When traveltime picks contain realistic levels of uncertainty—approximately 1.5 ms, corresponding to typical positioning errors in OBN surveys—spatial regularization alone produces spurious velocity features that obscure the true anomaly structure. Adding calendar-time smoothness constraints enables robust recovery of moving velocity anomalies even under these challenging conditions. The migration tests further validated the practical impact of accurate water-velocity models, showing measurable reductions in imaging artifacts when spatially varying corrections are applied rather than assuming a homogeneous water layer.

A key innovation in this work is the incorporation of spatially variable weights that encode prior knowledge about expected velocity variation patterns. Unlike previous approaches that impose rigid structural assumptions like a two-layered water model, the weighted regularization term provides flexible guidance without predetermining the solution's spatial structure. Field observations consistently show that water-velocity variations are most pronounced in the upper kilometer of the water column, while deeper regions remain relatively stable. By assigning larger weights to these deeper zones, the inversion is

encouraged to preserve background values where data constraints are weak, while permitting larger deviations in shallow regions where anomalies are both more likely and better illuminated by the acquisition geometry. This strategy proved particularly effective in the realistic synthetic examples, where weighted inversion reduced vertical smearing artifacts that would otherwise compromise the recovered velocity structure.

Several avenues for future development emerge from this work. The most immediate extension involves transitioning from the current 2D implementation to full 3D inversion. While computationally more demanding in terms of memory requirements and processing time, 3D treatment would capture the true acquisition geometry where velocity anomalies are illuminated from multiple azimuths as vessels traverse different sail lines. This reduced illumination per individual sail line compared to the repeated 2D geometry presents potential stability challenges given the increased number of model parameters. However, the temporal stabilization mechanism would become more effective in 3D, as the varying illumination angles across different acquisition times provide complementary constraints that the temporal regularization can leverage to improve overall solution quality.

Incorporating joint inversion for source and receiver position errors represents another important direction that would bring the methodology closer to industry practice. Position uncertainties contribute significantly to traveltime residuals and are routinely estimated alongside velocity in production workflows. Solving simultaneously for geometry corrections and water velocity introduces additional unknowns that could impact convergence and stability, but would provide a more complete treatment of the error sources affecting 4D repeatability. Understanding the trade-offs between these coupled parameters would yield valuable insights for acquisition design and processing strategies.

Finally, direct integration of auxiliary measurements could enhance model accuracy and resolution. Sound velocity profiler (SVP) data acquired during surveys provide ground-truth constraints at specific locations and times, yet the current framework only uses such information indirectly through the reference model and weights. Incorporating SVP mea-

surements as inequality constraints or through more sophisticated regularization terms would better exploit these high-quality observations. Similarly, oceanographic measurements of temperature and salinity, combined with empirical sound-speed relationships, could inform the expected magnitude and spatial distribution of velocity variations, leading to more consistent petrophysical solutions.

The framework developed here provides a foundation for addressing water-column challenges in time-lapse seismic monitoring, particularly in deep-water carbonate reservoirs where subtle 4D signals demand exceptional repeatability. As the industry continues expanding into complex offshore environments with significant oceanographic variability, methods that explicitly account for time-varying water properties will become increasingly critical for reliable reservoir surveillance.

REFERENCES CITED

Amini, A., H. Peng, Z. Zhang, R. Huang, and J. Yang, 2016, Joint inversion of water velocity and node position for ocean-bottom node data: SEG Technical Program Expanded Abstracts 2016, 5490–5494.

Araujo, R. C. F., G. Corso, H. A. D. do Nascimento, S. Xavier-de Souza, J. M. de Araujo, and T. Barros, 2024, Estimation of water velocity and receiver position changes in time-lapse seismic using machine learning: Brazilian Journal of Geophysics, **42**, 1–12; doi: 10.22564/brjg.v42i2.2313.

Bertrand, A., and C. MacBeth, 2005, Repeatability enhancement in deep-water permanent seismic installations: a dynamic correction for seawater velocity variations: Geophysical Prospecting, **53**, 229–242; doi: 10.1111/j.1365-2478.2004.00465.x.

Bishop, K., 2003, Lessons learned from the SMAART JV: Presented at the 65th EAGE Conference & Exhibition, EAGE.

Borges, F., M. Muzzette, L. E. Queiroz, B. Pereira-Dias, R. Dias, and A. Bulcão, 2022, Analysis of water velocity changes in time-lapse ocean bottom acquisitions - A synthetic 2D study in Santos Basin, offshore Brazil: Journal of Applied Geophysics, **197**, 104521; doi: 10.1016/j.jappgeo.2021.104521.

Carvill, C. V., 2009, A new approach to water velocity estimation and correction: Presented at the 71st EAGE Conference & Exhibition.

Hansen, P. C., 2010, Discrete inverse problems: Insight and algorithms: SIAM.

Hansen, P. C., and D. P. O'Leary, 1993, The use of the L-curve in the regularization of discrete ill-posed problems: SIAM Journal on Scientific Computing, **14**, 1487–1503.

Hatchell, P., H. Ruiz, A. Libak, B. Nolan, and R. Agersborg, 2019, Precise depth and subsidence measurements during deepwater OBN surveys: SEG Technical Program Expanded Abstracts 2019, Society of Exploration Geophysicists, 162–166.

IOC, SCOR, and IAPSO, 2010, The international thermodynamic equation of seawater – 2010: Calculation and use of thermodynamic properties: IOC Manuals and Guides No. 56, UNESCO.

Jervis, M., A. Bakulin, and R. Smith, 2018, Making time-lapse seismic work in a complex desert environment for CO_2 EOR monitoring – design and acquisition: The Leading Edge, **37**, 598–607; doi: 10.1190/tle37080598.1.

Johnston, D. H., 2013, Practical Applications of Time-lapse Seismic Data: Society of Exploration Geophysicists.

Kiyashchenko, D., W.-F. Wong, D. Cherief, D. Clarke, Y. Duan, and P. Hatchell, 2020, Unlocking seismic monitoring of stiff reservoirs with 4D OBN: A case study from Brazil pre-salt: SEG Technical Program Expanded Abstracts 2020, Society of Exploration Geophysicists, 3759–3763.

Lacombe, C., J. Schultzen, S. Butt, and D. Lecerf, 2006, Correction for water-velocity variations and tidal statics.

Li, Y., K. King, and T. Chen, 2016, Monitoring variations of seawater average velocity by using WBM from 4-C–4D OBS in GOM: SEG Technical Program Expanded Abstracts 2016, 5249–5253.

Lumley, D., D. Adams, M. Meadows, S. Cole, and R. Wright, 2005, 4D seismic data processing issues and examples: SEG Technical Program Expanded Abstracts, 1394–1397.

MacKay, S., J. Fried, and C. Carvill, 2003, The impact of water-velocity variations on deepwater seismic data: The Leading Edge, **22**, 344–350; doi: 10.1190/1.1572088.

Mackenzie, K. V., 1981, Nine-term equation for sound speed in the oceans: The Journal of the Acoustical Society of America, **70**, 807–812; doi: 10.1121/1.386920.

Mahgoub, M., Y. Bashir, A. A. Bery, and A. W. Noufal, 2023, 4D seismic co-processing pre-stack depth migration for scarce acquisition repeatability: Journal of Petroleum Exploration and Production Technology, **13**, 135–149; doi: 10.1007/s13202-022-01541-x.

Mitra, P. P., 2023, 4D seismic for reservoir management, *in* Developments in Structural Geology and Tectonics: Elsevier, **6**, 285–326.

Muijzert, E., C. Bagaini, A. Misbah, N. Seymour, M. Salgadoe, and B. Szydlik, 2022, Seismic Image Improvements after Correction for Errors in OBN Acquisition Parameters: 83rd EAGE Annual Conference & Exhibition, European Association of Geoscientists & Engineers, 1–5.

Osdal, B., and M. Landrø, 2011, Estimation of changes in water column velocities and thicknesses from time-lapse seismic data: Geophysical Prospecting, **59**, 295–309; doi: 10.1111/j.1365-2478.2010.00923.x.

Paffenholz, J., J. Stefani, B. McLain, and K. Bishop, 2002, Sigsbee_2a synthetic subsalt dataset – image quality as function of migration algorithm and velocity model error: Presented at the 64th EAGE Conference & Exhibition, EAGE.

Ritter, G. L. d. S., 2010, Water velocity estimation using inversion methods: GEOPHYSICS, **75**, U1–U8; doi: 10.1190/1.3280232.

Romero, J., M. Ravasi, and N. Luiken, 2022, Robust joint inversion and segmentation of 4D seismic data: SEG Technical Program Expanded Abstracts 2022, 3414–3418.

Seymour, N., C. Bagaini, E. Muyzert, K. Kapllan, and M. Salgadoe, 2021, Sparse OBN image improvements by correction for acquisition errors; doi: https://doi.org/10.1190/segam2021-3583604.1.

Udengaard, C. R., and K. Craft, 2012, Analysis of Water Column Complexity in OBN Data: Presented at the 74th EAGE Conference and Exhibition.

Wang, K., S. Dunn, J. Ward, and P. Hatchell, 2015, Direct measurement of water velocity and tidal variations for improved 4D repeatability in marine seismic acquisition: First Break, **33**, 73–79; doi: 10.3997/1365-2397.33.5.80180.

Wang, K., P. Hatchell, C. Udengaard, K. Craft, and S. Dunn, 2012, Direct measurement of water velocity and tidal variations in marine seismic acquisition: SEG Technical Program Expanded Abstracts 2012, 1–5.

———, 2013, Water velocity and tide measurement in marine seismic acquisition: Presented at the 75th EAGE Conference & Exhibition incorporating SPE EUROPEC 2013 — Extended Abstracts, European Association of Geoscientists & Engineers.

Xu, S., and D. Pham, 2003, Global solution to water column statics: A new approach to an old problem: SEG Technical Program Expanded Abstracts 2003, 2062–2065.

Zhang, D., C. Tsingas, A. A. Ghamdi, M. Huang, W. Jeong, K. K. Sliz, S. M. Aldeghaither, and S. A. Zahrani, 2021, A review of OBN processing: challenges and solutions: Journal of Geophysics and Engineering, **18**, 492–502; doi: 10.1093/jge/gxab024.